Journal of
Materials Chemistry B

PAPER

View Article Online
View Journal | View Issue

Cite this: *J. Mater. Chem. B*, 2023, **11**, 169

Halogen-free photosensitizers based on *meso*-enamine-BODIPYs for bioimaging and photodynamic therapy†

Ruth Prieto-Montero, ‡[a] Aitor Díaz Andres, ‡[b] Alejandro Prieto-Castañeda, ‡[c] Andrea Tabero,[d] Asier Longarte,[e] Antonia R. Agarrabeitia,[cf] Angeles Villanueva,[d] María J. Ortiz, [c] Raúl Montero,*[g] David Casanova *[bh] and Virginia Martínez-Martínez *[a]

Received 18th July 2022,
Accepted 23rd November 2022

DOI: 10.1039/d2tb01515c

rsc.li/materials-b

The search for efficient heavy atom free photosensitizers (PSs) for photodynamic therapy (PDT) is a very active field. We describe herein a simple and easily accessible molecular design based on the attachment of an enamine group as an electron-donor moiety at the *meso* position of the BODIPY core with different alkylation patterns. The effect of the alkylation degree and solvent polarity on the photophysical properties in terms of splitting absorption bands, fluorescence efficiencies and singlet oxygen production is analyzed in depth experimentally using spectroscopic techniques, including femtosecond and nanosecond transient absorption (fs- and ns-TA) and using computational simulations based on time-dependent density functional theory. The correlation between the theoretical/experimental results permits the rationalization of the observed photophysical behavior exhibited by *meso*-enamine-BODIPY compounds and the determination of mechanistic details, which rule the population of the triplet state manifold. The potential applicability as a theragnostic agent for the most promising compound is demonstrated through *in vitro* assays in HeLa cells by analyzing the internalization, localization and phototoxic action.

Introduction

The search for single systems able to diagnose and treat diseases, mainly cancer, has attracted great interest in modern medicine. Theragnosis (diagnosis and therapy) permits the *in situ* visualization of cancer tissues and cells, enhancing its treatment.[1–4] Nevertheless, searching for a theragnostic agent is not a trivial task.[5–9] A promising route could be the combination of fluorescence bioimaging for diagnosis and photodynamic therapy (PDT) as treatment, by the use of organic dyes.[4,10–16] PDT requires the presence of molecular oxygen (O_2), an organic dye (photosensitizer) and a specific light source. In PDT, the photosensitizer (PS) is activated under light, generating reactive oxygen species (ROS), mainly singlet oxygen ($^1O_2$), Fig. 1. This species of oxygen are cytotoxic and able to destroy cancer cells by apoptosis or necrosis.[17–19] However, fluorescence and ROS generation are competing photophysical processes and a suitable balance between these antagonistic features should be achieved.[20–23]

Recently, one type of new lab-made PS has been based on the BODIPY chromophore (boron dipyrromethene), considered a chemically versatile small chromophore with excellent photophysical properties (intense absorption and emission bands and high photoresistance), stable under physiological conditions and insensitive to environmental changes.[24–27] One strategy to design a theragnostic agent is the reduction of fluorescence by adding heavy atoms such as transition metals (Ru, Pd or Pt) or halogen atoms (Br or I) into the fluorophore structure, enhancing the intersystem crossing (ISC) driven by spin–orbit

---

[a] Departamento de Química Física, Facultad de Ciencia y Tecnología, Universidad del País Vasco/Euskal Herriko Unibertsitatea (UPV/EHU), 48080 Bilbao, Spain. E-mail: virginia.martinez@ehu.eus; Tel: +34-946-015-969
[b] Donostia International Physics Center (DIPC), 20018 Donostia, Euskadi, Spain
[c] Departamento de Química Orgánica, Facultad de CC. Químicas, Universidad Complutense de Madrid, 28040 Madrid, Spain
[d] Departamento de Biología, Universidad Autónoma de Madrid, Darwin 2, 28049 Madrid, Spain
[e] Spectroscopy Laboratory, Departamento Química Física, Facultad de Ciencia y Tecnología, Universidad del País Vasco/Euskal Herriko Unibertsitatea (UPV/EHU), Apartado 644, 48080 Bilbao, Spain
[f] Sección Departamental de Química Orgánica, Facultad de Óptica y Optometría, Universidad Complutense de Madrid, Arcos de Jalón 118, 28037 Madrid, Spain
[g] SGiker Laser Facility, Universidad del País Vasco (UPV/EHU), Sarriena s/n, 48940 Leioa, Spain
[h] IKERBASQUE, Basque Foundation for Science, 48009 Bilbao, Euskadi, Spain

† Electronic supplementary information (ESI) available. See DOI: **https://doi.org/10.1039/d2tb01515c**

‡ Equal contribution.

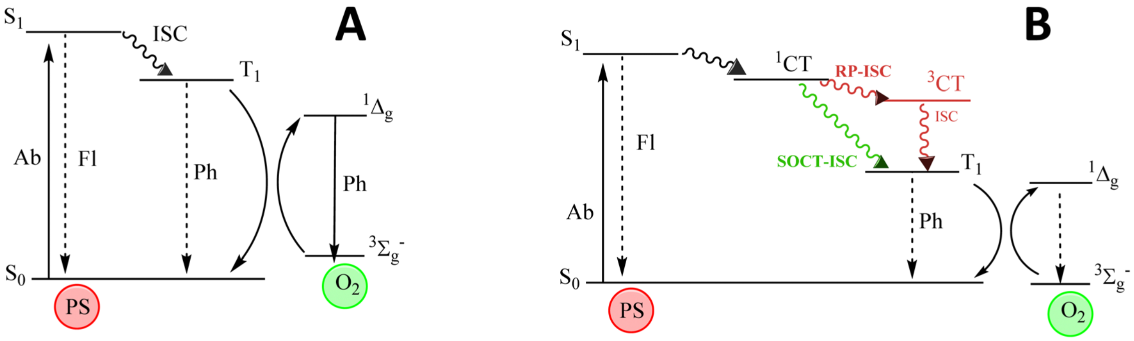

Fig. 1 Jablonski diagram showing the population of triplet states by the conventional intersystem crossing (ISC) mechanism from the first singlet excited state (A) and by radical-pair intersystem crossing (RP-ISC) or spin–orbit charge transfer intersystem crossing (SOCT-ISC) mechanisms (B).

coupling (SOC) and as a consequence, increasing the triplet state population,[19,20,22,28–32] Fig. 1A. For instance, upon addition of heavy atoms to the BODIPY core, especially iodinated atoms at 2 and 6 positions, its fluorescence drastically decreases in favor of the triplet state population by ISC ($S_1 \rightarrow T_n$), and high singlet oxygen generation is achieved.[18,20,24,31,33–39] Nevertheless, the efficiency of the photosensitizing action depends significantly on the lifetime of the lowest triplet state (T_1) and the presence of a heavy atom increases also the ISC process back to the ground state ($T_1 \rightarrow S_0$), considerably reducing the triplet state lifetime. Besides, halo-BODIPYs suffer from poor photostability and undesirable toxicity, diminishing their applicability and biocompatibility for biomedical uses.[18,19,37]

To address these drawbacks, the design of heavy atom-free photosensitizers is currently a very active research field.[40–53] One of the strategies relies on the combination of electron donor (D) and acceptor (A) moieties to induce charge transfer (CT) states, which can act as mediators between singlet and triplet excited states by two different pathways: radical pair intersystem crossing (RP-ISC)[54,55] or spin–orbit charge transfer intersystem crossing (SOCT-ISC),[56–59] Fig. 1B. Roughly, RP-ISC usually occurs when the electronic coupling between D and A units is weak, *e.g.*, in spatially separated dyads by a linker, whereas the SOCT-ISC efficiency rapidly decays with the distance and it often takes place in directly linked D–A structures with a nearly orthogonal disposition. Generally, by these types of mechanisms, singlet oxygen generation (triplet population) and fluorescence efficiency (singlet population) of PSs can be efficiently modulated by the relative electron ability of A and D units, their chemical connection and relative geometrical disposition, as well as the polarity of the media.[8,46,47,57,60–63]

Some examples of halogen-free BODIPYs, in which different electron-donor groups have been incorporated into the chromophore core,[39,45,47,48,53,63–67] have been already reported as potential theragnostic agents. In most cases, the electron-donating unit is added to the *meso* position, considering the most sensitive one in terms of the photophysical impact because of the marked change in the electronic density that occurs upon excitation (Fig. 2-Top).

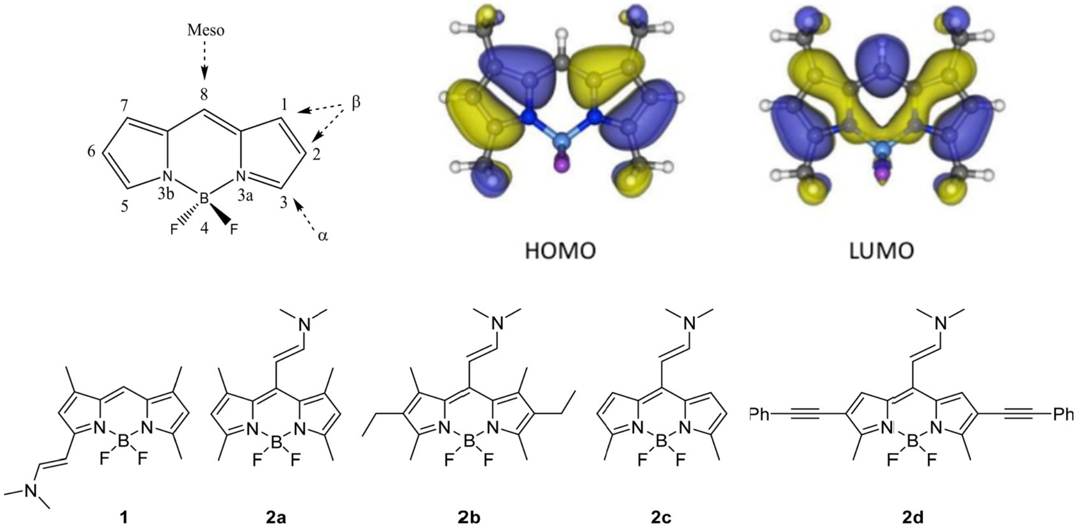

Fig. 2 (Top) General BODIPY structure. The different positions in the core are indicated and numbered according to the IUPAC system.[68] Frontier orbitals involved in the lowest electronic transitions (HOMO and LUMO) of a representative BODIPY; Bottom) Molecular structures of the different enamine substituted BODIPY derivatives.

In this work, unlike other previous studies, a small group, an enamine, is selected as electron donor substituent in the set of studied BODIPYs shown in Fig. 2.[39,45,48,53,63,65–67,69] All these compounds were synthesized using the Vilsmeier–Haack reaction, showing a new family of structurally simple and easily accessible compounds with push–pull character.[70] First, the effect exerted on photophysics by the substitution of this group at the α- *vs.* *meso*-positions of the BODIPY core is compared (**1** *vs.* **2a** in Fig. 2-Bottom). Then, in the search for the best fluorescent-PS agent for PDT, several *meso*-enamine-BODIPY derivatives varying the alkylation pattern of the BODIPY core are analyzed (**2a**–**2c**, Fig. 2-Bottom). The effects of the alkylation degree and solvent polarity on the resultant photophysical features are deeply analyzed by theoretical simulations that allow characterizing the electronic states involved in the excitation/relaxation processes. To further understand the observed photophysical behavior, the relaxation pathway and the energy of the involved states were explored by femtosecond and nanosecond transient absorption (TA) and triplet energy and lifetime characterization. Finally, the collected evidence allows us to postulate a new BODIPY, with ethynyl phenyl groups at 2- and 6-positions to extend the delocalization of the π-system (**2d** in Fig. 2), as a suitable candidate with a red-shifted absorption band for theragnostic applications. The internalization, localization and phototoxic action of this compound are tested *in vitro* in HeLa cells with very promising results.

Table 1 Photophysical properties and singlet oxygen quantum yield in chloroform for enamine-BODIPY compounds; absorption maxima (λ_{ab}), molar absorption coefficient (ε_{max}), fluorescence maxima (λ_{fl}), fluorescence quantum yield (Φ_{fl}), fluorescence lifetime (τ_{fl}) and singlet oxygen quantum yield (Φ_{Δ})

Compound	λ_{ab} (nm)	ε_{max} 10^{-4} (M^{-1} cm^{-1})	λ_{fl} (nm)	Φ_{fl}	$\tau_{fl}{}^{a}$ (ns)	Φ_{Δ}
1	575	4.3	593	0.60	0.69 (10%) 4.04 (90%)	0
2a	494/451	5.7	518/640	< 0.01	—	0.04
2b	516/449	3.3	540/670	< 0.01	—	0
2c	496/460	6.6	529	0.08	0.92 (97%) 5.29 (3.0%)	0.20
2d	551/490	5.7	599	0.42	3.23	0.31

[a] λ_{ex} = 530 nm, λ_{em} = 585 nm (for **1**); λ_{ex} = 480 nm, λ_{em} = 530 nm (for **2c**); λ_{ex} = 490 nm, λ_{em} = 600 nm (for **2d**).

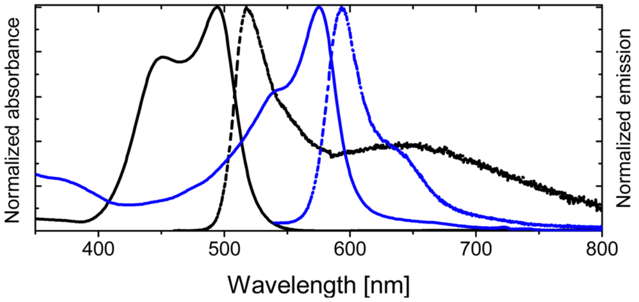

Fig. 3 Height-normalized absorption (solid curves) and emission spectra (dash curves) in chloroform for **1** (blue) *vs.* **2a** (black).

Results and discussion

Enamine substitution of BODIPY

First, the impact of the position of the donor enamine group on the photophysical properties was analyzed by comparing the enamine-BODIPYs substituted at the 3- or *meso*-position (**1** *vs.* **2a**). As expected, the enamine substitution at the α-position extends the π-conjugation of the BODIPY core, as shown by the π-electron distribution of the highest occupied molecular orbital (HOMO) and the lowest unoccupied molecular orbital (LUMO) (Fig. S1, ESI†), which induces a bathochromic shift with respect to the unsubstituted green BODIPYs, placing their respective absorption and emission bands in the orange region of the visible spectra (575 nm and 593 nm, respectively, Table 1). The relative shift in the absorption bands of **1** and **2a** is well recovered by the computed vertical excitations at the Franck–Condon region (Table S1, ESI†). Compound **1** keeps a relatively high fluorescence quantum yield (60%) and negligible singlet oxygen production (Fig. 3 and Table 1).

Conversely, by simply attaching the enamine group at the *meso* position, the photophysical properties of the BODIPY are drastically changed. Compound **2a** brings an important difference in the location of their respective spectroscopic bands, and it shifted to shorter wavelengths with respect to compound **1** (Table 1 and Fig. 3). This hypsochromic effect is typically found when electron donor groups are anchored in the *meso* position, especially for amine groups.[71,72] Moreover, the absorption spectra, unlike common BODIPY dyes, show an important shoulder contribution at shorter wavelengths, placed at around 450 nm. The formation of H-type aggregates is discarded as the spectrum is registered in a diluted solution ($\sim 2 \times 10^{-6}$ M). The nature of this contribution will be discussed in detail below. Besides, the enamine substitution at the *meso* position induces drastic fluorescence emission quenching, shortening its lifetime (Table 1). Although the fluorescence is weak for **2a** (Table 1), it was possible to record a dual emission (Fig. 3 and Table 1), showing a narrower emission band at 518 nm assigned to the locally excited (LE) state and a broader band centered at around 640 nm, characteristic of radiative deactivation of an intramolecular charge transfer (CT) state.[73,74] Although the presence of an enamine unit at the *meso* position in compound **2a** enhances the non-radiative deactivation pathways, the triplet state is not effectively populated, yielding relatively low singlet oxygen production (4% in chloroform, Table 1).

Role of alkylation in *meso*-enamine substituted BODIPYs

Further alkylation of the BODIPY core with two extra ethyl groups at 2,6-positions, compound **2b**, does not ameliorate the photophysical properties (Table 1), rendering practically null fluorescence and singlet oxygen production in all solvents of any polarity (Table 1 and Table S3, ESI†). Intriguingly, the absorption spectrum of compound **2b** clearly shows two independent bands, with the peak centered at shorter wavelengths slightly blue-shifted with respect to the previously denoted as a shoulder for compound **2a**. Contrarily, the main absorption band is red-shifted with respect to that recorded for the homologous compound **2a** (Table 1 and Fig. 4A). The splitting of the two absorption bands of **2b** increases as the polarity of the solvent decreases (Fig. 4B). Decreasing the polarity of the solvent, acetonitrile > chloroform > toluene > *c*-hexane, has a double effect on the absorption peak at shorter wavelengths, that is, a gradual intensity decrease and a hypsochromic shift. On the other hand, the main absorption band (at higher wavelengths) suffers a bathochromic shift and becomes progressively more intense. Indeed, for apolar solvents, *e.g.*, *c*-hexane, the absorption bands are nicely divided into two distinguished peaks. In contrast, in polar solvents, *e.g.*, acetonitrile, both absorption contributions overlap as they become closer in energy and intensity.

To gain insight into the nature of the two bands in the absorption spectra, rationalize the differences between the studied compounds and understand the changes induced by the polarity of the solvent, we have carried out electronic structure calculations for molecules **2a–c**. The ground state energy minimum of molecule **2b** exhibits a relative torsion of $\theta \sim 30^\circ$ between the group at the *meso* position and BODIPY's molecular plane. Nonplanarity is promoted by steric hindrance of the enamine with the methyl groups at positions 1 and 7. TDDFT calculations at the Franck–Condon geometry identify the two lowest singlet-to-singlet electronic transitions in **2b** as optically active, *i.e.*, with large oscillator strengths, in good agreement with the presence of two absorption bands registered in solution (Fig. 4). The lowest excited singlet state is mainly obtained as the excitation from the HOMO to the LUMO, whereas S_2 can be described as the electronic promotion from the HOMO−1 to the LUMO (Fig. 5a). The HOMO of **2b** is localized on the BODIPY unit, while HOMO−1 emerges from the coupling of the enamine and BODIPY π-systems. Finally, the LUMO is largely delocalized over both enamine and BODIPY moieties.

Interestingly, frontier orbital energies change with the polarity of the environment. Concretely, solvents with larger dielectric constants stabilize and destabilize the HOMO and HOMO−1, respectively (Fig. 5b and c). On the other hand, the energy of the LUMO remains rather constant. As a consequence, the transition energy to S_1 (S_2) increases (decreases) with the solvent polarity, and the S_1 to S_2 energy gap decreases. It is worth noting that the computed oscillator strengths (f) suggest a change in the relative intensity of the two bands, with the $f(S_2)/f(S_1)$ ratio increasing with the polarity of the solvent (Table 2). These results explain the change in the absorption profiles upon the change in the solvent polarity, *i.e.*, the frequency shift of the two bands and the change in relative intensities (Fig. 4B).

Dealkylation of positions 2 and 6 in **2a** with respect to **2b** preserves the torsion of the enamine with respect to the BODIPY fragment. The main difference between the electronic structures of **2a** and **2b** is the orbital energy of the HOMO, since it is the frontier orbital presenting the largest electron density at the 2 and 6 carbon atoms. Substitution of the alkyl groups by a more electronegative hydrogen stabilizes the HOMO (Fig. S2, ESI†), shifting the S_1 transition to shorter wavelengths and reducing the energy separation between the S_1 and S_2 states (Table 3), in agreement with the absorption spectra (Fig. 4A). Similarly, dealkylation of positions 1 and 7 in **2c** mainly stabilizes the HOMO and LUMO, as both orbitals present sizeable electron densities on these atoms. As a consequence, the S_1 energy barely changes with respect to **2a**, while the S_2 transition slightly redshifts ($\sim$ 0.1 eV), resulting in a rather small separation between the S_1 and S_2 transitions. In fact, the absorption spectrum of **2c** does not show a noticeable shoulder feature at shorter wavelengths and the main band resembles the one for pristine BODIPY (no substitution). It is worth noting that the no-alkylation in 1 and 7 atoms slightly increases the molecular planarity in **2c** ($\theta \sim 26^\circ$) with respect to **2b** and **2a**, allowing for larger electronic mixing of the BODIPY and enamine π-systems (Fig. S1, ESI†).

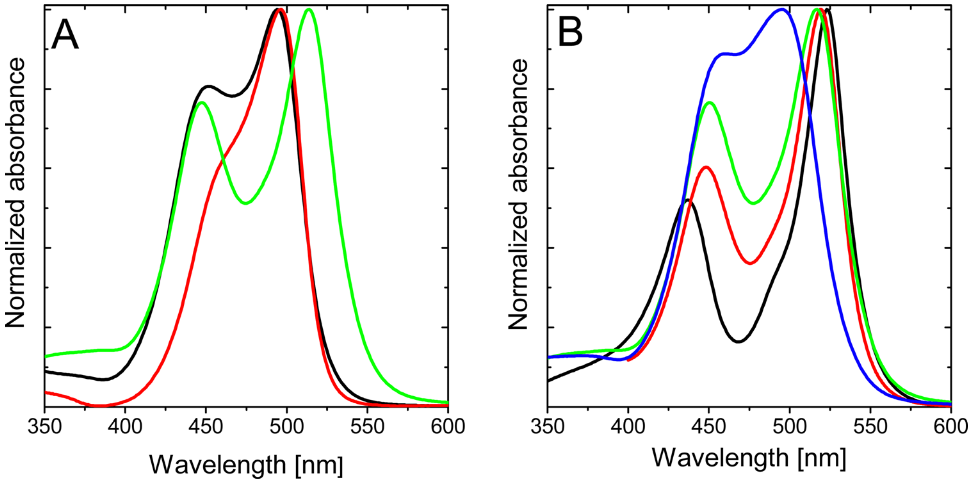

Fig. 4 (A) Normalized absorption spectra of **2a** (black), **2b** (green) and **2c** (red) in chloroform; and (B) normalized absorption spectra of **2b** in different solvents: *c*-hexane (black), toluene (red), chloroform (green) and acetonitrile (blue).

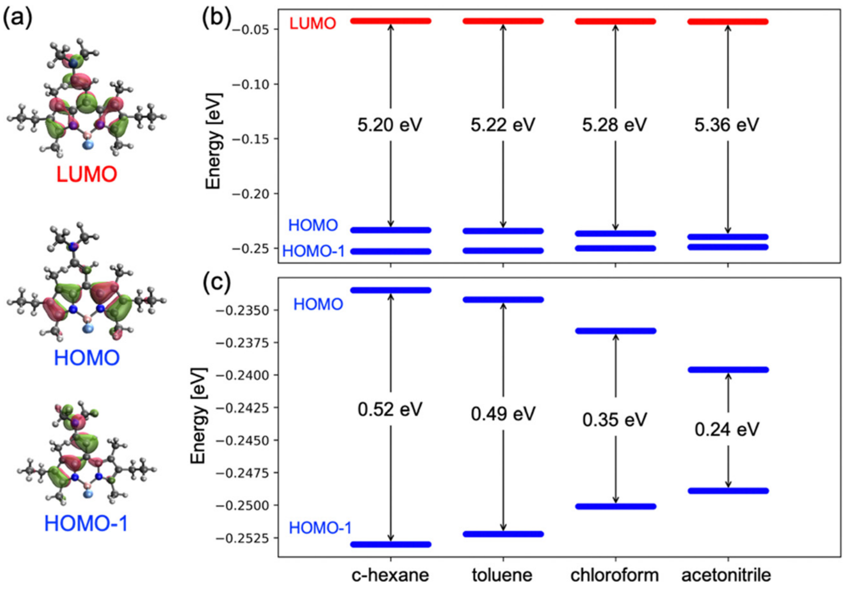

Fig. 5 (a) Frontier molecular orbitals of **2b** computed with CAM-B3LYP/cc-pVDZ in chloroform. (b) Orbital energy diagram (in eV) of **2b** in *c*-hexane, toluene, chloroform and acetonitrile. (c) Zoom of HOMO and HOMO−1 orbital energies.

Table 2 Vertical excitation energies (in eV) to S_1 and S_2 for compound **2b** computed at the CAM-B3LYP/cc-pVDZ level in different solvents: *c*-hexane, toluene, chloroform, and acetonitrile. Oscillator strengths of the transitions are indicated in parentheses. ΔE (in eV) is the S_1 to S_2 energy separation

Solvent	$E(S_1)$	$E(S_2)$	ΔE
c-Hexane	2.86 (0.635)	3.32 (0.588)	0.46
Toluene	2.88 (0.628)	3.30 (0.599)	0.42
Chloroform	2.90 (0.624)	3.22 (0.651)	0.32
Acetonitrile	2.98 (0.569)	3.21 (0.649)	0.23

Table 3 Vertical excitation energies (in eV) to S_1 and S_2 for compounds **2a**, **2b** and **2c** computed at the CAM-B3LYP/cc-pVDZ level in chloroform. Oscillator strengths of the transitions are indicated in parentheses. ΔE (in eV) is the S_1 to S_2 energy separation

Molecule	$E(S_1)$	$E(S_2)$	ΔE
2b	2.90 (0.624)	3.22 (0.651)	0.32
2a	3.00 (0.585)	3.25 (0.635)	0.25
2c	3.02 (0.559)	3.12 (0.692)	0.10

On the other hand, regarding the fluorescence and singlet oxygen quantum yield, our results clearly indicate that methylation at 1- and 7-positions in *meso*-enamine-BODIPYs noticeably influences the fluorescence efficiency, and more significantly, the singlet oxygen generation (Table 1 and Table S3, ESI†). Compound **2c**, without methyl groups at 1- and 7-positions, shows the highest singlet oxygen and fluorescence quantum yields of the series, whereas compounds **2a** and **2b** show nearly no emission and singlet oxygen production, being internal conversion (IC) the main deactivation pathway (see next section). Moreover, the fluorescence quantum yield and also the singlet oxygen quantum yield of **2c** increase as the polarity of the solvent decreases (Table S3, ESI†). The less efficient radiative deactivation of the singlet excited state, as well as the singlet to triplet transition in polar solvents, was also observed for other BODIPY dyads.[47,57,60]

Decay dynamics of photoactivated enamine-BODIPYs

In order to extract mechanistic information on the excited state relaxation of the present compounds, TA experiments have been carried out on **2b** (Fig. 6) and **2c** (Fig. 7), considering them as representative examples in terms of methylation degree, in solvents with different polarities (toluene, $CHCl_3$ and ACN). Fig. 6a shows the TA spectra of **2b** in toluene at selected pump-probe delays. At short delays (0.15 ps) the TA spectrum is composed mainly of 3 contributions: a positive band at 350–400 nm attributable to excited state absorption (ESA), the ground state bleach (GSB) at 425–525 nm and a lower negative feature extending from 525 to 700 nm and corresponding to stimulated emission (SE). The blue end of the latter contribution reflects the emission from the initially prepared excited state. It decays in 1 ps, denoting a short living LE state. Within the same time scale, a positive feature appears at 570 nm corresponding to the absorption from an excited species formed during the LE state decay. A comparison with previous studies on BODIPY donor and acceptor groups[75] allows us to identify this feature as the absorption of a CT state, in which the enamine plays the role of the donor and the BODIPY core acts as the acceptor. The remarkable red shift of the emission during the first picoseconds seems to support this hypothesis.

A multiexponential fit with four components (τ_1 = 1.1 ps; τ_2 = 19 ps; τ_3 = 118 ps; τ_4 > 5 ns) yields a satisfactory description of the transient spectra. The distribution of pre-exponential factors resulting from this analysis is presented in the decay associated spectra (DAS) in Fig. 6b (see the ESI† for further details on data analysis). As is observed there, for **2b** the

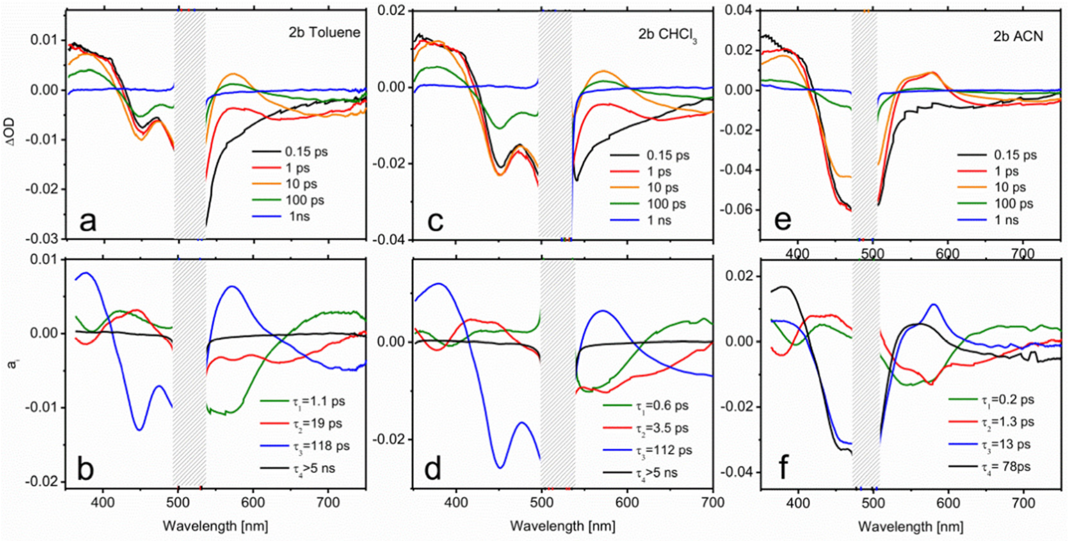

Fig. 6 Transient spectra and DAS of **2b** in toluene (a and b), $CHCl_3$ (c and d) and ACN (e and f).

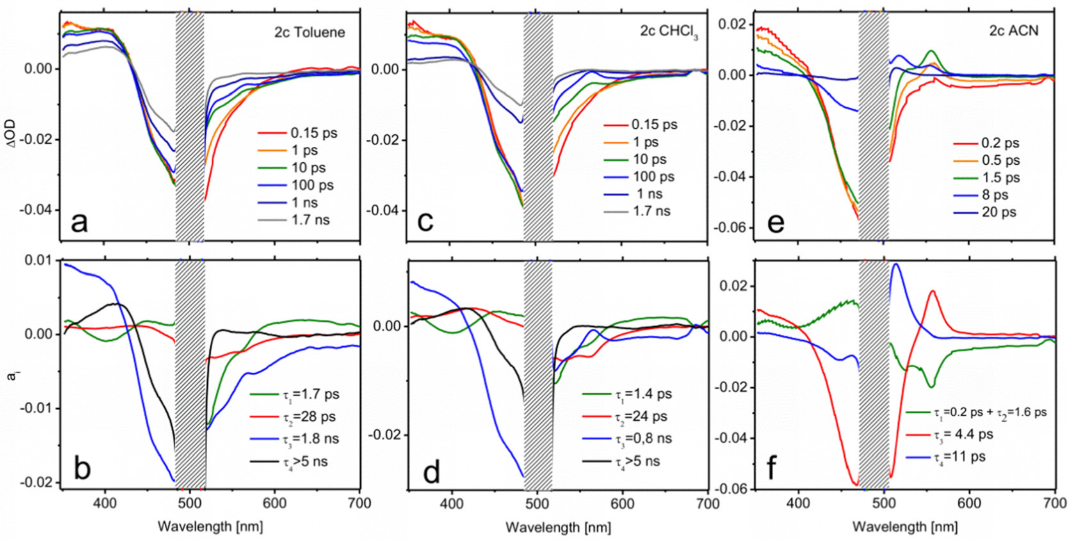

Fig. 7 Transient spectra and DAS of **2c** in toluene (a and b), $CHCl_3$ (c and d) and ACN (e and f).

amplitude of the slower decay (a_4) is negligible, but it is included for the latter comparison with **2c**. The distribution of a_1 (τ_1 = 1.1 ps) shows changes in the ESA band without affecting the evolution of the GSB, meaning that the nature of the excited state is modified in this time scale. Indeed, a_1 describes simultaneously the LE emission decay (550 nm) and the onset of the CT features (positive band at 570 nm and emission at wavelengths > 650 nm). Therefore, a_1 accounts for the population that is initially excited to S_1 (LE), and reaches the CT state. Regarding τ_3, as displayed by the GSB band, the excited state population decays to the ground state with 118 ps lifetime. The spectral characteristics of the CT state in the 500–700 nm region are also perceptible in the a_3 distribution, which indicates that IC to the ground state mainly occurs from the CT state. Finally, the scrutiny of a_2 reflects that certain CT formation takes place in a slower time scale (τ_2 = 19 ps). In fact, a_1 and a_2 spectra are very similar except for the emission contribution in the red edge. Differently, a_2 shows emission at intermediate wavelengths between the LE and CT bands, which could be related to the cooling (vibrational relaxation) on the CT potential well.

A higher polarity solvent such as $CHCl_3$ (panels c and d in Fig. 6) does not change qualitatively the dynamics, as illustrated by the resemblance of the transient spectra and DAS with those in the previous solvent. Only a substantial acceleration of CT formation is noticeable. Thus, in $CHCl_3$, τ_1 and τ_2 are respectively 0.6 and 3.5 ps, while IC remains almost unaltered (τ_3 = 112 ps). Following the same trend, Fig. 6e and f show that further stabilization of the CT state with a higher-polarity solvent (ACN) gives rise to even faster dynamics (τ_1 = 0.2 ps; τ_2 = 1.3 ps; τ_3 = 13 ps; τ_4 = 78 ps). In this case, two components of tens of picoseconds, τ_3 and τ_4, account for the independent radiationless relaxation pathways of the CT state. The origin of these dual deactivation channels to the ground state is unclear.

Although notable differences in the kinetics are observed for **2c**, its TA data (Fig. 7) can be understood by the same basic model as that employed for **2b**. In toluene, the decay of the LE fluorescence and the onset of the red shifted emission of the CT formation take place in τ_1 = 1.7 ps and τ_2 = 28 ps, respectively (Fig. 7b). The decay of the CT state, described by the a_3 spectrum, is much slower in this case (τ_3 = 1.8 ns). It is also worth noting that the CT emission in **2c** covers the 520–600 nm region, pointing to a less marked CT character. Indeed, the CT absorption band at 570 nm appears now as a small dip on top of the emission band. The most remarkable feature in the relaxation of **2c** is the appearance of a very long-living species ($\tau_4 > 5$ ns) that can be identified as the T_1 state on the basis of its TA spectrum (a_4). This triplet state has to be formed from the CT relaxation, although its formation dynamics cannot be resolved from the recorded data. The triplet quantum yield can be determined on the grounds of the a_4 component through the ratio between the GSB band maximum in the a_4 spectrum and at t = 0 ns, yielding a value of Φ_T = 0.37. This number is in total agreement with the singlet oxygen quantum yield obtained in this solvent by the direct registration of its photoluminescence signal (Table S3, ESI†). Moreover, the assignation of the TA spectrum at $\tau_4 > 5$ ns to the triplet state absorption features is confirmed by the registration of the TA spectra in the nanosecond range (Fig. S3, ESI†). Similarly, the ns-resolved TA (ns-TA) presents a positive band around 375–430 nm, attributed to the absorption of the T_1 state, a negative contribution in the 425–525 nm range that corresponds to ground state bleaching (GSB) associated with $S_0 \rightarrow S_1$ transition, and a weak and broad contribution at > 525 nm, also assigned to triplet absorption.[47,60,74,76,77] The lifetimes registered at 405 nm and 540 nm measured under nitrogen-saturated conditions were 16 μs, long enough for efficient oxygen quenching (Fig. S3, ESI†). The spin-triplet multiplicity nature of this state is confirmed by quenching registered within the triplet lifetime range under aerated conditions (Table S4, ESI†).

The CT dynamics of **2c** in $CHCl_3$ is very similar. However, its lifetime is noticeably shorter (τ_3 = 0.8 ns) and the triplet quantum yield is lower (Φ_T = 0.24), which is once again in agreement with the singlet oxygen production obtained in this solvent. This fact suggests that the formation of a long-lived CT state is required in order to efficiently couple to the triplet state. The ns-TA spectrum is comparable to that obtained in toluene (Fig. S3, ESI†), but a much longer triplet lifetime is registered (113 μs, Table S4, ESI†). Finally, in ACN, extremely fast relaxation of the CT is observed (panels e and f in Fig. 7 and Fig. S5, ESI†). The formation of the CT state occurs at a similar scale (τ_1 = 0.2 ps and τ_2 = 1.6 ps), both of which, owing to their very similar spectra, have been plotted together in Fig. 7f for simplicity. However, the subsequent decay is much faster, draining the population to the ground state with τ_3 = 4.4 ps. This channel precludes the formation of a triplet state. Accordingly, the distribution of a_4 is compatible with the cooling of the excitation energy in the ground state (vibrational relaxation) that is now perceptible due to the very fast IC.

Further experiments were also carried out for **2b** and **2c** in $CHCl_3$ using excitation energies resonant with the S_2 state (445 nm). The observed dynamics was essentially the same recorded after pumping to S_1, pointing to a very fast S_2–S_1 conversion in both species (Fig. S6, ESI†).

ISC mechanism

TA measurements of **2b** and **2c** indicate that the triplet state population occurs from a CT state, suggesting a SOCT mechanism. Electronic structure calculations of **2c** identify two excited state minima on the S_1 potential energy surface. At small torsion angles between BODIPY and the *meso*-enamine fragments, there is a local S_1 minimum with the hole and electron largely localized on the BODIPY and with the participation of enamine's π-system, which can be related to the LE state identified by TA spectroscopy (Fig. 8). The LE geometry exhibits a small enamine-BODIPY dihedral angle (∼ 20°) and presents a sizeable transition dipole moment and oscillation strength to the ground state (Table S2, ESI†). Hence, we identify it as the state responsible for the fluorescence emission recorded in the 500–540 nm region. Additionally, the molecule presents a lower energy excited state minimum with an orthogonal disposition between the two fragments in which the hole is localized on the enamine unit and the electron on the

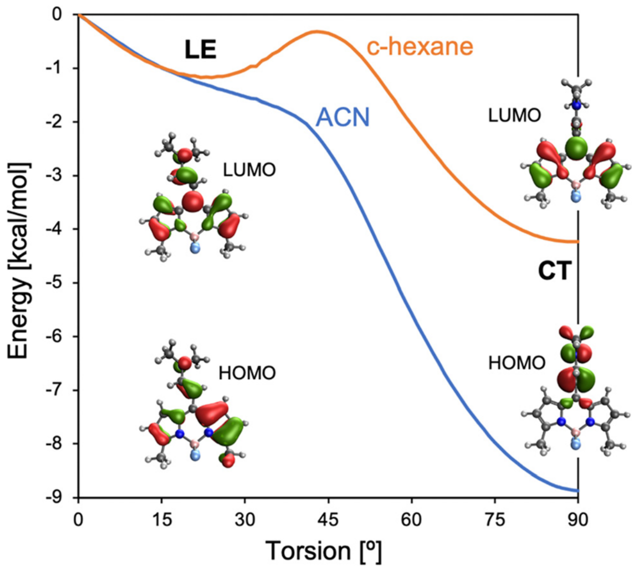

Fig. 8 Energy profiles (in kcal mol^{-1}) of the lowest excited singlet state (S_1) of **2c** computed in *c*-hexane (orange) and ACN (blue) along the molecular torsion between BODIPY and enamine moieties. The molecular torsion model has been obtained by constrained geometry optimization of the S_1 state in ACN at different torsion angles. S_1 energies are relative to the value in the planar arrangement. Inset: HOMO and LUMO for LE and CT states.

BODIPY fragment, *i.e.*, a CT state. Notably, the relative energy between LE and CT states strongly depends on the solvent polarity, with polar solvents stabilizing the orthogonal CT with respect to the LE state. The vertical energy gap to the ground state at the CT minimum severely diminishes upon increasing the polarity of the solvent (Table S2, ESI†), in line with the increase of non-radiative decay rates and the hindering of singlet oxygen generation.

At the LE minimum, although the S_1 state presents non-vanishing SOCs to the two lowest triplet states, singlet–triplet energy gaps are rather large, preventing efficient ISC, as in pristine BODIPY (Fig. 9). On the other hand, molecular torsion towards the CT minimum largely reduces S_1/T_n energy differences and modifies the electronic nature of low-lying states. Along the molecular orthogonalization, T_1 strongly localizes on the BODIPY moiety, whereas T_2 becomes a purely CT excitation, like the lowest excited singlet. As a consequence, in the perpendicular arrangement S_1/T_2 nearly degenerates and presents a small SOC, in accordance with El Sayed's rule. Simultaneously, the S_1/T_1 energy gap (SOC) decreases (increases) considerably. We note that despite the reduction of the singlet–triplet gap, it remains rather large (Fig. 9a). On the other hand, it is well-known that TDDFT functionals tend to underestimate and overestimate the energies of T_1 and S_1, respectively.[78] Therefore, these results make us conclude that ISC in **2b** (and **2c**) is triggered by excited state relaxation *via* BODIPY-enamine torsion, and takes place through the SOCT-ISC mechanism between the CT excited singlet and low-lying triplets, in particular the BODIPY-localized T_1 state, but also the second excited triplet T_2.

To further characterize the energy of the lowest triplet state (T_1), luminescence measurements are recorded at 78 K for **2c** (Fig. S7, ESI†). The band placed at 655 nm was assigned to phosphorescence emission, with average lifetimes in the ms range. The energy of this low-lying triplet state (182.8 kJ mol^{-1}) is higher than the energy gap between the triplet ground state of O_2 ($^3\Sigma_g$) and the first singlet excited state ($^1\Delta_g$) of O_2 (94.2 kJ mol^{-1}), fulfilling the necessary conditions to generate singlet oxygen by the type-II energy transfer mechanism (Fig. 1). With **2c** being the best compound of the series in terms of singlet oxygen quantum production and fluorescence efficiency, a more π-conjugated *meso*-enamine BODIPY, Fig. 2, **2d**, was formulated. By attaching ethynyl phenyl groups at 2 and 6 positions a notable shift takes place in both absorption and emission bands (Fig. S8, ESI†), resulting in an even better balance between fluorescence and singlet oxygen quantum yields (Table 1 and Table S1, ESI†), and showing a relatively long lived triplet state close to 100 μs (Fig. S4 and Table S4, ESI†). Hence, **2d** could be considered as a purely organic agent with a suitable balance between fluorescence and singlet oxygen capacities with potential use in theragnostic applications.

In vitro tests

Compound **2d** was selected as the most suitable enamine-BODIPY to perform assays in HeLa cells. Subcellular localization experiments confirm that **2d** can be internalized inside cells, allowing sharp fluorescence imaging following a typical lipid droplet pattern, indicative of selective accumulation (Fig. 10A). Taking into account the broad fluorescence emission spectrum of compound **2d**, it was not possible to carry out colocalization experiments with commercial organelle-targeted fluorescent probes, since the emissions of probes and compound **2d** would overlap. However, Fig. S9 (ESI†) shows that the subcellular distribution pattern of compound **2d** is absolutely similar to that of lipid droplets, and besides, quite different from mitochondria or lysosomes in HeLa cells. Interestingly, the fluorescence image obtained with **2d** is much sharper and brighter than compound **1**, besides its lower fluorescence efficiency (Table 1).

Given the better performance of **2d** in cellular internalization, we selected this compound for further experiments in order to assess its phototoxicity. After 24 h of incubation with **2d** and 10 J cm^{-2} irradiation with 518 nm light, HeLa cell viability was evaluated using an MTT assay. The results shown below (Fig. 10) demonstrate that **2d** induces high phototoxicity after green irradiation at low light doses (10 J cm^{-2}) even at the lowest **2d** concentration assayed (98% of cell death at 1 μM). Null or very low dark toxicity was detected under our experimental conditions.

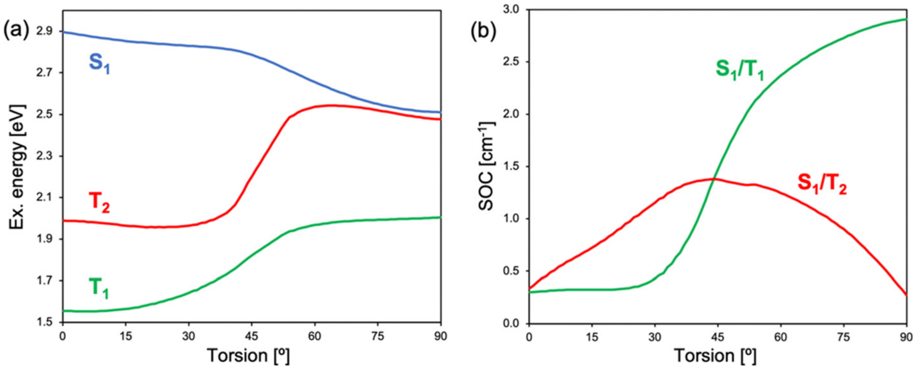

Fig. 9 (a) Excitation energy (in eV with respect to the ground state at the planar geometry) of the lowest excited singlet (S_1) and triplet (T_1 and T_2) states and (b) singlet/triplet SOCs computed in ACN of **2c** along the molecular torsion between BODIPY and enamine moieties.

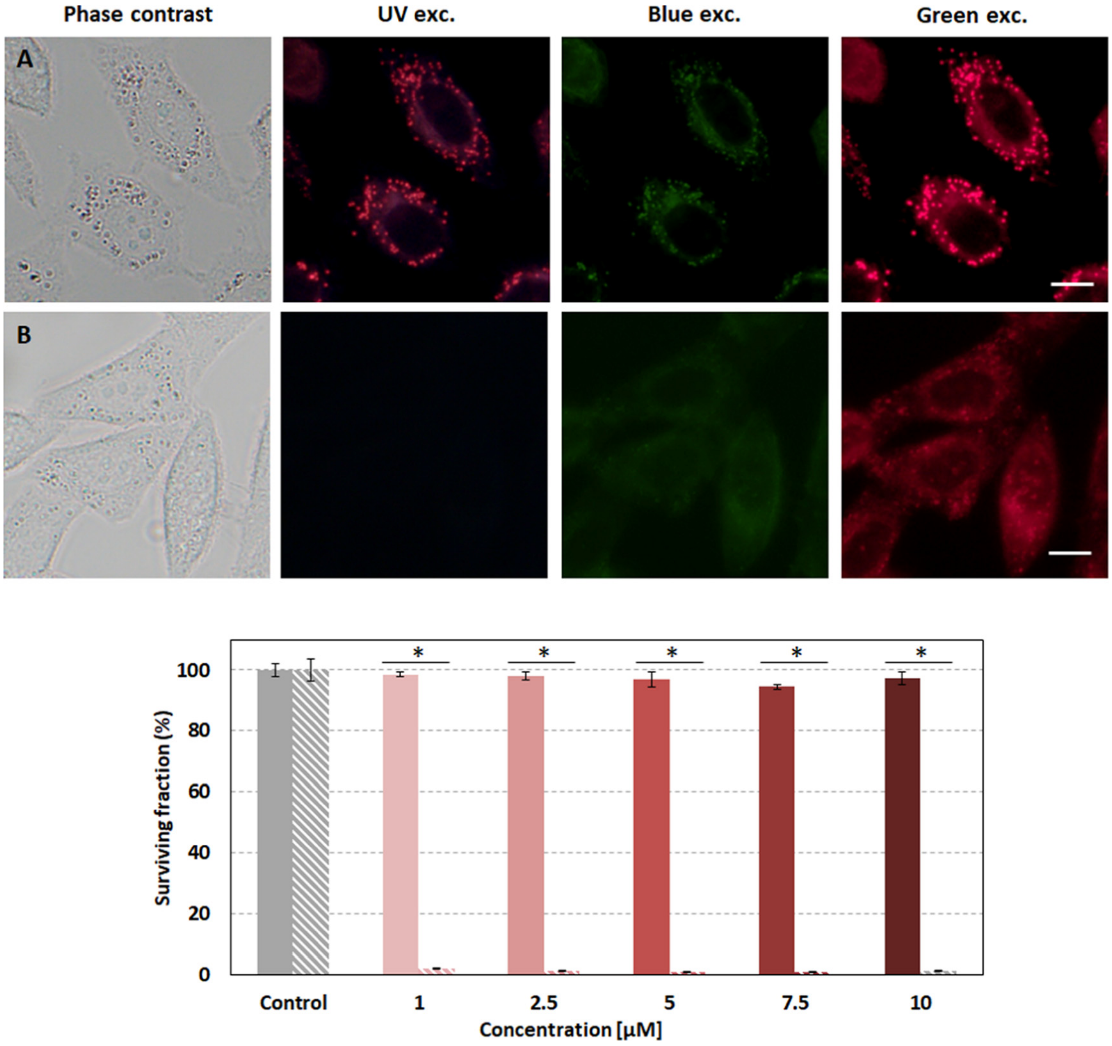

Fig. 10 (Top) Fluorescence microscopy images of HeLa cells incubated with **2d** (A) and **1** (B). Bottom) MTT assay results of **2d** under dark conditions (striped bars) and green irradiation (plain bars; 10 J cm^{-2}). Scale bar: 10 µm. Statistical significance for the surviving fraction was obtained by using one-way ANOVA. Statistically significant differences are labelled as * ($p < 0.001$).

Conclusions

This study evidences that *meso*-enamine-BODIPYs are a new family of structurally simple and easily accessible BODIPYs with the capability to act as halogen-free $^1O_2$ photosensitizers for PDT or even for theragnosis based on PDT and fluorescence. The attachment of an enamine group (electron-donor) at the *meso* position activates a charge transfer state, the key to populate the triplet state *via* SOCT-ISC. This mechanism is triggered by excited state relaxation *via* BODIPY-enamine torsion (towards orthogonalization), taking place between the CT excited singlet and low-lying triplets, in particular the BODIPY-localized T_1 state, but also the second excited triplet T_2.

Theoretical simulations and experimental characterization of the excited state relaxation by femto-transient absorption demonstrated that the formation and energetic stabilization of a CT state induce a faster deactivation kinetics, promoted by the polarity of the solvent and/or alkylation of the BODIPY core (mainly at 1- and 7-positions), accelerate non-radiative decay rates hindering singlet oxygen generation and fluorescence ability. In fact, the CT state must be formed with a sufficient lifetime (timescale set at $\geq$ 1.8 ns) to allow the population of triplet states.

The rational design of a *meso*-enamine BODIPY without alkylation at C1 and C7, but with extended conjugation at C2 and C6, has demonstrated its viability as a biomarker of lipid droplets and a photosensitizer agent in HeLa cells being very photoefficient at low green light doses (10 J cm^{-2}) and low concentrations ($\leq$ 1 µM) and no cytotoxic under dark conditions.

Further studies to explore the possibility of the development of red-absorbing photosensitizers based on the present strategy (enamine group at the *meso* position of the BODIPY core) by the introduction of larger extended π-conjugated moieties at C2 and C6 and/or at C3 and C5 positions would be interesting to research.

Data availability

All of the additional information and experimental data are provided in the ESI.†

Author contributions

A.P.-C., A. R. A. and M. J. O. synthesized and chemically characterized all compounds. R. P.-M. and V. M.-M. measured the photophysical properties. A. L. and R. M. carried out the femtosecond measurements. A. D. A. and D. C. performed the theoretical simulations. A. T. and A. V. conducted the *in vitro* assays. R. M., D. C. and V. M.-M. wrote the manuscript. V. M.-M. revised and edited the final manuscript. V. M.-M. conceived and supervised the study. All authors have read and agreed to the published version of the manuscript.

Conflicts of interest

There are no conflicts to declare.

Acknowledgements

This work was funded by MCIN/AEI/10.13039/501100011033 (projects no. PID2020-114347RB-C32, PID2020-114755GB-C31, PID2019-109555GB-I00 and RED2018-102815-T) and Gobierno Vasco (project no. IT1639-22 and PIBA19-0004). R. P.-M. and A. D. A. thank UPV/EHU, MIU and NGEU for their respective postdoctoral (MARSA21/71) and predoctoral (PRE2020-092036) fellowships. We also thank the SGIker Laser Facility of the UPV/EHU for technical support.

References

1 S. S. Kelkar and T. M. Reineke, *Bioconjugate Chem.*, 2011, **22**, 1879–1903.

2 A. Yordanova, E. Eppard, S. Kürpig, R. A. Bundschuh, S. Schönberger, M. Gonzalez-Carmona, G. Feldmann, H. Ahmadzadehfar and M. Essler, *OncoTargets Ther.*, 2017, **10**, 4821–4828.

3 S. Navalkissoor, G. Gnanasegaran and R. Baum, *Br. J. Radiol.*, 2018, **91**, 20189004.

4 D. van Straten, V. Mashayekhi, H. de Bruijn, S. Oliveira and D. Robinson, *Cancers*, 2017, **9**, 19–73.

5 E. K. Lim, T. Kim, S. Paik, S. Haam, Y. M. Huh and K. Lee, *Chem. Rev.*, 2015, **115**, 327–394.

6 R. Kumar, W. S. Shin, K. Sunwoo, W. Y. Kim, S. Koo, S. Bhuniya and J. S. Kim, *Chem. Soc. Rev.*, 2015, **44**, 6670–6683.

7 W. Hu, H. Ma, B. Hou, H. Zhao, Y. Ji, R. Jiang, X. Hu, X. Lu, L. Zhang, Y. Tang, Q. Fan and W. Huang, *ACS Appl. Mater. Interfaces*, 2016, **8**, 12039–12047.

8 W. Hu, X. Miao, H. Tao, A. Baev, C. Ren, Q. Fan, T. He, W. Huang and P. N. Prasad, *ACS Nano*, 2019, **13**, 12006–12014.

9 B. Yang, Y. Chen and J. Shi, *Adv. Mater.*, 2019, **31**, 1901778.

10 X. Li, S. Kolemen, J. Yoon and E. U. Akkaya, *Adv. Funct. Mater.*, 2017, **27**, 1604053.

11 B. del Rosal, B. Jia and D. Jaque, *Adv. Funct. Mater.*, 2018, **28**, 1803733.

12 C. N. Ko, G. Li, C. H. Leung and D. L. Ma, *Coord. Chem. Rev.*, 2019, **381**, 79–103.

13 M. DeRosa, *Coord. Chem. Rev.*, 2002, **233–234**, 351–371.

14 C. Hopper, *Lancet Oncol.*, 2000, **1**, 212–219.

15 K. Moghissi, K. Dixon and S. Gibbins, *Surg. J.*, 2015, **01**, e1–e15.

16 H. T. Bui, D. K. Mai, B. Kim, K.-H. Choi, B. J. Park, H.-J. Kim and S. Cho, *J. Phys. Chem. B*, 2019, **123**, 5601–5607.

17 D. E. J. G. J. Dolmans, D. Fukumura and R. K. Jain, *Nat. Rev. Cancer*, 2003, **3**, 380–387.

18 B. Kim, B. Sui, X. Yue, S. Tang, M. G. Tichy and K. D. Belfield, *Eur. J. Org. Chem.*, 2017, 25–28.

19 C. S. Kue, S. Y. Ng, S. H. Voon, A. Kamkaew, L. Y. Chung, L. V. Kiew and H. B. Lee, *Photochem. Photobiol. Sci.*, 2018, **17**, 1691–1708.

20 A. Kamkaew, S. H. Lim, H. B. Lee, L. V. Kiew, L. Y. Chung and K. Burgess, *Chem. Soc. Rev.*, 2013, **42**, 77–88.

21 G. Durán-Sampedro, N. Epelde-Elezcano, V. Martínez-Martínez, I. Esnal, J. Bañuelos, I. García-Moreno, A. R. Agarrabeitia, S. de la Moya, A. Tabero, A. Lazaro-Carrillo, A. Villanueva, M. J. Ortiz and I. López-Arbeloa, *Dyes Pigm.*, 2017, **142**, 77–87.

22 S. Zhen, S. Wang, S. Li, W. Luo, M. Gao, L. G. Ng, C. C. Goh, A. Qin, Z. Zhao, B. Liu and B. Z. Tang, *Adv. Funct. Mater.*, 2018, **28**, 1706945.

23 P. R. Ogilby, *Chem. Soc. Rev.*, 2010, **39**, 3181–3209.

24 N. Boens, B. Verbelen, M. J. Ortiz, L. Jiao and W. Dehaen, *Coord. Chem. Rev.*, 2019, **399**, 213024–213109.

25 A. Treibs and F.-H. Kreuzer, *Justus Liebigs Ann. Chem.*, 1968, **718**, 208–223.

26 F. López Arbeloa, J. Bañuelos, V. Martínez, T. Arbeloa and I. López Arbeloa, *Int. Rev. Phys. Chem.*, 2005, **24**, 339–374.

27 X. F. Zhang and J. Zhu, *J. Lumin.*, 2019, **205**, 148–157.

28 R. Prieto-Montero, A. Prieto-Castañeda, R. Sola-Llano, A. R. Agarrabeitia, D. García-Fresnadillo, I. López-Arbeloa, A. Villanueva, M. J. Ortiz, S. Moya and V. Martínez-Martínez, *Photochem. Photobiol.*, 2020, **96**, 458–477.

29 R. Padrutt, V. Babu, S. Klingler, M. Kalt, F. Schumer, M. I. Anania, L. Schneider and B. Spingler, *ChemMedChem*, 2020, 694–701.

30 J. Zhao, K. Xu, W. Yang, Z. Wang and F. Zhong, *Chem. Soc. Rev.*, 2015, **44**, 8904–8939.

31 T. Yogo, Y. Urano, Y. Ishitsuka, F. Maniwa and T. Nagano, *J. Am. Chem. Soc.*, 2005, **127**, 12162–12163.

32 I. S. Turan, G. Gunaydin, S. Ayan and E. U. Akkaya, *Nat. Commun.*, 2018, **9**, 805.

33 W. Wu, Y. Geng, W. Fan, Z. Li, L. Zhan, X. Wu, J. Zheng, J. Zhao and M. Wu, *RSC Adv.*, 2014, **4**, 51349–51352.

34 S. G. Awuah and Y. You, *RSC Adv.*, 2012, **2**, 11169–11183.

35 J. H. Gibbs, Z. Zhou, D. Kessel, F. R. Fronczek, S. Pakhomova and M. G. H. Vicente, *J. Photochem. Photobiol., B*, 2015, **145**, 35–47.

36 R. Lincoln, A. M. Durantini, L. E. Greene, S. R. Martínez, R. Knox, M. C. Becerra and G. Cosa, *Photochem. Photobiol. Sci.*, 2017, **16**, 178–184.

37 J. Zou, Z. Yin, K. Ding, Q. Tang, J. Li, W. Si, J. Shao, Q. Zhang, W. Huang and X. Dong, *ACS Appl. Mater. Interfaces*, 2017, **9**, 32475–32481.

38 A. J. Sánchez-Arroyo, E. Palao, A. R. Agarrabeitia, M. J. Ortiz and D. García-Fresnadillo, *Phys. Chem. Chem. Phys.*, 2017, **19**, 69–72.

39 A. Turksoy, D. Yildiz and E. U. Akkaya, *Coord. Chem. Rev.*, 2019, **379**, 47–64.

40 V. N. Nguyen, Y. Yan, J. Zhao and J. Yoon, *Acc. Chem. Res.*, 2021, **54**, 207–220.

41 Y. Dong, A. Elmali, J. Zhao, B. Dick and A. Karatay, *Chem. Phys. Chem.*, 2020, **21**, 1388–1401.

42 J. W. Verhoeven, *J. Photochem. Photobiol., C*, 2006, **7**, 40–60.

43 Z. J. Jakubek, M. Chen, M. Couillard, T. Leng, L. Liu, S. Zou, U. Baxa, J. D. Clogston, W. Y. Hamad and L. J. Johnston, *J. Nanopart. Res.*, 2018, **20**, 98.

44 Y. Zhao, R. Duan, J. Zhao and C. Li, *Chem. Commun.*, 2018, **54**, 12329–12332.

45 X. F. Zhang and N. Feng, *Chem. – Asian J.*, 2017, **12**, 2447–2456.

46 Z. Wang, M. Ivanov, Y. Gao, L. Bussotti, P. Foggi, H. Zhang, N. Russo, B. Dick, J. Zhao, M. Di Donato, G. Mazzone, L. Luo and M. Fedin, *Chem. – Eur. J.*, 2020, **26**, 1091–1102.

47 J. Jiménez, R. Prieto-Montero, B. L. Maroto, F. Moreno, M. J. Ortiz, A. Oliden-Sánchez, I. López-Arbeloa, V. Martínez-Martínez and S. de la Moya, *Chem. – Eur. J.*, 2020, **26**, 601–605.

48 W. Hu, Y. Lin, X. F. Zhang, M. Feng, S. Zhao and J. Zhang, *Dyes Pigm.*, 2019, **164**, 139–147.

49 T. C. Pham, S. Heo, V. N. Nguyen, M. W. Lee, J. Yoon and S. Lee, *ACS Appl. Mater. Interfaces*, 2021, **13**, 13949–13957.

50 V. N. Nguyen, S. J. Park, S. Qi, J. Ha, S. Heo, Y. Yim, G. Baek, C. S. Lim, D. J. Lee, H. M. Kim and J. Yoon, *Chem. Commun.*, 2020, **56**, 11489–11492.

51 L. A. Ortiz-Rodríguez and C. E. Crespo-Hernández, *Chem. Sci.*, 2020, **11**, 11113–11123.

52 V. N. Nguyen, S. Heo, C. W. Koh, J. Ha, G. Kim, S. Park and J. Yoon, *ACS Sens.*, 2021, **6**, 3462–3467.

53 W. Hu, X.-F. Zhang and M. Liu, *J. Phys. Chem. C*, 2021, **125**, 5233–5242.

54 X. Wang, Y. Song, G. Pan, W. Han, B. Wang, L. Cui, H. Ma, Z. An, Z. Xie, B. Xu and W. Tian, *Chem. Sci.*, 2020, **11**, 10921–10927.

55 E. A. Weiss, M. A. Ratner and M. R. Wasielewski, *J. Phys. Chem. A*, 2003, **107**, 3639–3647.

56 D. Liu, A. M. El-Zohry, M. Taddei, C. Matt, L. Bussotti, Z. Wang, J. Zhao, O. F. Mohammed, M. Di Donato and S. Weber, *Angew. Chem., Int. Ed.*, 2020, **59**, 11591–11599.

57 M. A. Filatov, *Org. Biomol. Chem.*, 2019, **18**, 10–27.

58 D. J. Gibbons, A. Farawar, P. Mazzella, S. Leroy-Lhez and R. M. Williams, *Photochem. Photobiol. Sci.*, 2020, **19**, 136–158.

59 Y. Dong, A. A. Sukhanov, J. Zhao, A. Elmali, X. Li, B. Dick, A. Karatay and V. K. Voronkova, *J. Phys. Chem. C*, 2019, **123**, 22793–22811.

60 X. F. Zhang and X. Yang, *J. Phys. Chem. B*, 2013, **117**, 9050–9055.

61 E. Bassan, A. Gualandi, P. G. Cozzi and P. Ceroni, *Chem. Sci.*, 2021, **12**, 6607–6628.

62 L. A. Ortiz-Rodríguez, S. J. Hoehn, A. Loredo, L. Wang, H. Xiao and C. E. Crespo-Hernández, *J. Am. Chem. Soc.*, 2021, **143**, 2676–2681.

63 A. A. Buglak, A. Charisiadis, A. Sheehan, C. J. Kingsbury, M. O. Senge and M. A. Filatov, *Chem. – Eur. J.*, 2021, **27**, 9934–9947.

64 S. Rihn, P. Retailleau, N. Bugsaliewicz, A. De Nicola and R. Ziessel, *Tetrahedron Lett.*, 2009, **50**, 7008–7013.

65 M. A. Filatov, S. Karuthedath, P. M. Polestshuk, S. Callaghan, K. J. Flanagan, T. Wiesner, F. Laquai and M. O. Senge, *ChemPhotoChem*, 2018, **2**, 606–615.

66 Y. Dong, B. Dick and J. Zhao, *Org. Lett.*, 2020, **22**, 5535–5539.

67 J. Zhao, K. Chen, Y. Hou, Y. Che, L. Liu and D. Jia, *Org. Biomol. Chem.*, 2018, **16**, 3692–3701.

68 J. B. Prieto, F. L. Arbeloa, V. M. Martínez, T. A. López and I. L. Arbeloa, *J. Phys. Chem. A*, 2004, **108**, 5503–5508.

69 M. A. Filatov, S. Karuthedath, P. M. Polestshuk, H. Savoie, K. J. Flanagan, C. Sy, E. Sitte, M. Telitchko, F. Laquai, R. W. Boyle and M. O. Senge, *J. Am. Chem. Soc.*, 2017, **139**, 6282–6285.

70 E. Palao-Utiel, L. Montalvillo-Jiménez, I. Esnal, R. Prieto-Montero, A. R. Agarrabeitia, I. García-Moreno, J. Bañuelos, I. López-Arbeloa, S. de la Moya and M. J. Ortiz, *Dyes Pigm.*, 2017, **141**, 286–298.

71 I. Esnal, I. Valois-Escamilla, C. F. A. Gómez-Durán, A. Urías-Benavides, M. L. Betancourt-Mendiola, I. López-Arbeloa, J. Bañuelos, I. García-Moreno, A. Costela and E. Peña-Cabrera, *Chem. Phys. Chem.*, 2013, **14**, 4134–4142.

72 V. P. Yakubovskyi, M. P. Shandura and Y. P. Kovtun, *Dyes Pigm.*, 2010, **87**, 17–21.

73 N. Epelde-Elezcano, E. Palao, H. Manzano, A. Prieto-Castañeda, A. R. Agarrabeitia, A. Tabero, A. Villanueva, S. de la Moya, Í. López-Arbeloa, V. Martínez-Martínez and M. J. Ortiz, *Chem. – Eur. J.*, 2017, **23**, 4837–4848.

74 Y. Liu, J. Zhao, A. Iagatti, L. Bussotti, P. Foggi, E. Castellucci, M. Di Donato and K. L. Han, *J. Phys. Chem. C*, 2018, **122**, 2502–2511.

75 R. Montero, V. Martínez-Martínez, A. Longarte, N. Epelde-Elezcano, I. Lamas and I. L. Arbeloa, *J. Phys. Chem. Lett.*, 2021, **12**, 7439–7441.

76 Y. Lee, R. M. Malamakal, D. M. Chenoweth and J. M. Anna, *J. Phys. Chem. Lett.*, 2020, **11**, 877–884.

77 Q. Zhou, M. Zhou, Y. Wei, X. Zhou, S. Liu, S. Zhang and B. Zhang, *Phys. Chem. Chem. Phys.*, 2017, **19**, 1516–1525.

78 V. Postils, F. Ruipérez and D. Casanova, *J. Chem. Theory Comput.*, 2021, **17**, 5825–5838.